Journal of Applied Geophysics 153 (2018) 7–16

Contents lists available at ScienceDirect

Journal of Applied Geophysics

journal homepage: www.elsevier.com/locate/jappgeo

Joint TEM and MT aquifer study in the Atacama Desert, North Chile

Alexander D. Ruthsatz[a], Alvaro Sarmiento Flores[b], Daniel Diaz[c], Pablo Salazar Reinoso[b], Cristian Herrera[b], Heinrich Brasse[a,*]

[a] Freie Universität Berlin, Fachrichtung Geophysik, Malteserstr. 74-100, Berlin 12249, Germany
[b] Universidad Católica del Norte, Departamento de Ciencias Geológicas, Av. Angamos 610, Antofagasta, Chile
[c] Universidad de Chile, Departamento de Geofísica, Av. Blanco Encalada 2002, Santiago, Chile

ARTICLE INFO

Article history:
Received 27 April 2017
Received in revised form 14 January 2018
Accepted 3 April 2018
Available online 11 April 2018

Keywords:
Magnetotellurics
Time domain electromagnetics
Aquifer
Profeta Basin
Atacama Desert
Chile
South America

ABSTRACT

The Atacama Desert represents one of the driest regions on earth, and despite the absence of sustainable clean water reserves the demand has increased drastically since 1970 as a result of growing population and expanding mining activities. Magnetotelluric (MT) and Transient Electromagnetic (TEM) measurements were carried out for groundwater exploration in late 2015 in the area of the Profeta Basin at the western margin of the Chilean Precordillera. Both methods complement each other: While MT in general attains larger penetration depths, TEM allows better resolution of near surface layers; furthermore TEM is free from galvanic distortion. Data were collected along three profiles, enabling a continuous resistivity image from the surface to at least several hundred meters depth. TEM data were inverted in a 1-D manner, consistently yielding a poorly conductive near-surface layer with a thickness of approximately 30 m and below a well-conducting layer which we interpret as the aquifer with resistivities around 10 Ωm. At marginal sites of the main SW-NE-profile the resistive basement was found in 150 m. These depths are confirmed by interpretation of the MT soundings. Those were firstly inverted with a 2-D approach and then by 3-D inversion as clear indications of three-dimensionality exist. Several modeling runs were performed with different combinations of transfer functions and smoothing parameters. Generally, MT and TEM results agree reasonably well and an overall image of the resistivity structures in the Profeta Basin could be achieved. The aquifer reaches depths of more than 500 m in parts and, by applying Archie's law, resistivities of 1 Ωm can be assumed, indicating highly saline fluids from the source region of the surrounding high Andes under persisting arid conditions.

1. Introduction

The Atacama Desert of Chile and Peru represents one of the driest regions on earth and therefore water resource management and exploration represent crucial factors regarding a sustainable economy. According to the UN-Water Country Brief Chile (2013), withdrawal from the industry has tripled since 1975 and to this day governmental expenditures for the development of water supply, sanitation as well as hydroelectric power generation have constantly increased. Especially the area around the city of Antofagasta shows increasing demand as a result of growing population and expanding mining activities. Only few publicly accessible water resource exploration surveys have been conducted and hence an extensive aquifer study was initiated by the Universidad Católica del Norte, Antofagasta in collaboration with the Universidad de Chile, Santiago and the Freie Universität Berlin, funded by the CONICYT Educational Research Center. Various groups involved shall acquire inter alia data from geophysical, hydrogeological and geochemical studies.

MT and TEM measurements were carried out in the context of groundwater exploration in September and October 2015 in the area of the Profeta Basin in the Atacama Desert, North Chile (see Fig. 1). The study area is located midway between the cities of Antofagasta and Taltal at roughly 24.9°S, 69.5°W and at an altitude of about 2400 to 2800 m at the margin of the Chilean Precordillera. In March 2015, the area was affected by untypical heavy rain.

The name "Profeta Basin" (or Profeta-La Ternera Basin) had been used to describe the Late Triassic-Jurassic backarc basin and its marine sedimentary deposits by Chong (1977), Chong and von Hillebrandt (1985) and citations therein; in recent times, authors have used the name "Quebrada del Profeta Basin (Ravine of Profeta Basin)" when discussing the Cenozoic, continental sedimentary, intramontane basin (Fernández-Mort et al., 2015) that is described

* Corresponding author.
E-mail address: heinrich.brasse@fu-berlin.de (H. Brasse).

https://doi.org/10.1016/j.jappgeo.2018.04.002
0926-9851/

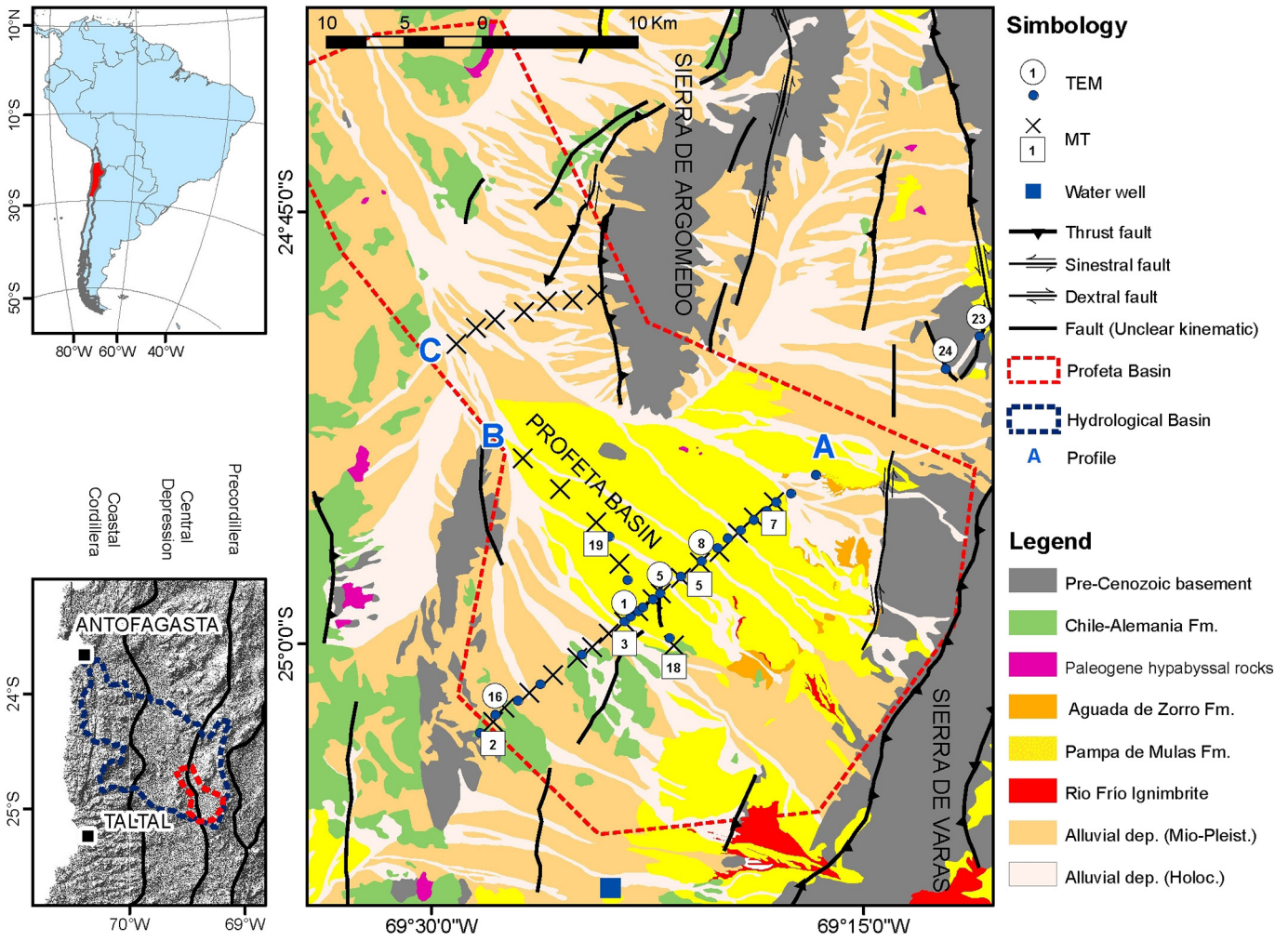

Fig. 1. Location map. Upper left: The study area at the South American margin. Lower left: Major morphostructural elements in the North of Chile with nearby cities. Right: Geological map of the Profeta Basin, including locations of the MT-TEM sites and a water well in the south of the basin (modified from Espinoza et al., 2011; Espinoza et al., 2012; Venegas et al., 2013; González et al., 2015).

in this present work. Because the Triassic-Jurassic strata are beyond the scope of this work, in this context "Profeta Basin" will also refer to the Cenozoic basin.

2. Geological setting

2.1. Tectonic context

In the Andean orogen one may differentiate morphostructural units orientated parallel to the strike of the range. The continuity of these units is interrupted in regions where oceanic ridges intersect the continental margin and corresponds to flat-slab subduction zones, causing segmentation of the orogen and the absence of the Central Depression, a morphological unit that separates the Coastal Cordillera from Main Cordillera. In the regions outside of the flat-slab segments, the Wadati-Benioff zone is steeper, as in the segment between 18° and 27°S (Charrier et al., 2007). The influence of the uplifting of the Andean orogen manifests in the forearc by the existence of major strike-slip fault systems parallel to the orogen in the Precordillera zone, with shortening normal to the orogen (Reutter et al., 1991) and with the development of several sedimentary basins, mostly continental, distributed through the major morphostructural units of the forearc in the north of Chile. The Domeyko Fault System (DFS) is located in the Precordillera and presents structures that evidence a complex history with several deformation events which have influenced the evolution of the Profeta Basin. The major uplifting of the Precordillera occurred during the Incaic Phase of the Andean Cycle, between 50 and 30 Ma (Charrier et al., 2007), when the transpressional geometry for the area was also developed; after this tectonic event at least two reactivations have been recognized (González et al., 2015).

2.2. Stratigraphy

The basement of the basin is formed by rocks of Carboniferous to Eocene age, including pyroclastic, volcanic, siliciclastic and plutonic rocks. The most recent rocks of the basement correspond to the Chile-Alemania Formation, consisting of volcanic and pyroclastic rocks of rhyolitic and dacitic composition (Paleocene to Early Eocene, 65–48 Ma), and small outcrops of hypabyssal rocks of andesitic composition (58 Ma) (González et al., 2015).

The sedimentary filling of the basin corresponds to Aguada de Zorro Formation, Pampa de Mulas Formation, Río Frío Ignimbrite and alluvial deposits. Aguada de Zorro Fm. (Eocene to Oligocene) is composed of partially to totally cemented gravels and conglomerates, and represents a fluvio-lacustrine system, with its source in the west and with more lacustrine facies on the eastern limit of its outcrops (Fernández-Mort et al., 2015). A minimum thickness of

150 m has been estimated for this unit; paleosoils of arid environments (Calcisoils and Gypsysoils) have been observed at the upper limit of this formation (González et al., 2015). Pampa de Mulas Fm. is composed of poorly selected, semi-consolidated gravels and coarse sands of Upper Oligocene to Middle Miocene age. Its origin has been estimated as alluvial fans with a drainage direction from east to west (Fernández-Mort et al., 2015). A minimum thickness of approximately 100 m has been estimated. Río Frío Ignimbrite is interbedded in Pampa de Mulas Fm.; this ignimbrite has been observed with an average thickness of 10 m in the area (Venegas et al., 2013). The most recent units of the sedimentary filling correspond to alluvial deposits of Miocene-Pleistocene and Holocene age, the combined thickness of both units has been recorded as maximal 15 m (González et al., 2015).

2.3. Hydrogeology

The Profeta Basin is located at the eastern limit of the La Negra hydrological basin, extending from the Precordillera to the coast (DGA, 2012). Isotopic similarities between water from springs located in the Pre- and Coastal Cordilleras suggest that the recharge zone is located in the Sierra de Varas (Herrera and Custodio, 2014). The flow of subterranean water is controlled mainly by the permeability contrast between basement and sedimentary filling, in some places related to structural control, manifested as fault-controlled uplifting of basement and the development of tectonic traps filled with Neogene sediments (González et al., 2015).

Herrera et al. (1997) described an unconfined aquifer consisting of the sedimentary filling of the Profeta Basin including the Río Frío Ignimbrite, that achieves, locally, a high secondary permeability through fracturing; and also identified water on the fractured siliciclastic basement rocks on the east margin of the basin; this, added to the register of fractures on the Chile-Alemania Fm. Gamboa (2014) evidence the fracturing of the basement. This is relevant because of the higher elevation of the Sierra de Varas cause that the sporadic recharge occurs in this zone, firstly through basement units (Herrera et al., 1997).

3. MT and TEM principles

Aquifers are often (but not always) characterized by low electrical resistivities due to conductive fluid in the interconnected pore space. Exploration methods usually include geoelectric sounding; however, high contact resistances and essential long electrode offsets severely limit its application. To overcome these restrictions, we applied a combination of the transient electromagnetic (TEM) and the magnetotelluric (MT) sounding methods.

3.1. Response functions

MT and TEM differ in their origin of the source signal, the measured field components and most importantly the domain of the considered variables. MT is based on the so-called magnetotelluric impedance Z, a variable of frequency, being defined as the ratio of orthogonal, horizontal electric and magnetic field components. The linear relation of the electric field E and magnetic field B is given as

$$\begin{bmatrix} E_x \\ E_y \end{bmatrix} = \begin{bmatrix} Z_{xx} & Z_{xy} \\ Z_{yx} & Z_{yy} \end{bmatrix} \begin{bmatrix} B_x \\ B_y \end{bmatrix} \tag{1}$$

The impedance contains information about the electrical properties of the subsurface. From the impedance we can extract the apparent resistivity ρ_a in Ωm and the impedance phase ϕ in degrees as transfer functions:

$$\rho_a(\omega) := \frac{\mu}{\omega} |Z|^2 \tag{2}$$

$$\phi(\omega) := arg(Z) = arctan\frac{\Im(Z)}{\Re(Z)} \tag{3}$$

Here ω denotes angular frequency and μ the magnetic permeability.

MT presumes a quasi-stationary and a quasi-homogeneous field. The decay of the field and therefore the depth of investigation scales with the skin or penetration depth δ which can be approximated by

$$\delta \approx \frac{1}{2}\sqrt{\rho T}, \quad [\delta] = km \tag{4}$$

where T denotes period and ρ the resistivity of a homogeneous halfspace.

The vertical magnetic field B_z also allows for the calculation of a magnetic transfer function:

$$B_z = \begin{bmatrix} W_x & W_y \end{bmatrix} \cdot \begin{bmatrix} B_x \\ B_y \end{bmatrix} = W_x B_x + W_y B_y \tag{5}$$

$[W_x\ W_y]$ is referred to as the tipper as the magnetic field vector tips out of the horizontal plane and is a complex function of the frequency. The in- and out-of-phase parts yield the induction arrows:

$$\vec{P} := \Re(W_x \vec{e}_x) + \Re(W_y \vec{e}_y) \tag{6}$$

$$\vec{Q} := \Im(W_x \vec{e}_x) + \Im(W_y \vec{e}_y) \tag{7}$$

where $\vec{e}_x$ and $\vec{e}_y$ are the unit vectors. Typically, the induction arrows adequately indicate lateral conductivity variations, as $\vec{P}$ points away from the conductivity anomaly in a two-dimensional environment. $\vec{Q}$ is normally not taken into account as it changes sign at specific frequencies (in a 2-D setting where $\vec{P}$ is maximal).

TEM as an active method supplies electric currents via a transmitter (often a rectangular coil). After turning off the transmitting signal, the decay of the induced currents in the subsurface can be measured with one or more receivers at the surface. Decay and diffusion are variables of time and subject to the conductivity distribution. Inferences on the geological – in this case particularly hydrogeological – setting can be achieved by implementation of the correspondent mathematical statements. According to Zhdanov (2009), definition of the TEM response functions is 'neither standard nor obvious' as apparent resistivity splits into an early and late part:

$$\rho_{a,early}(t) = \frac{R^3}{3\,A\,n} V_{coil} \tag{8}$$

$$\rho_{a,late}(t) = \left(\frac{I\,R^2\,A\,n}{20\,V_{coil}} \sqrt{\frac{\mu_0^5}{\pi\,t^5}} \right)^{\frac{2}{3}} \tag{9}$$

where R denotes the separation between receiver and transmitter (for an in-loop square configuration the distance from the center to the outer loop, equal to half of the outer sides of the transmitter square). A is the effective area in square meters, n the number of turns, V_{coil} refers to the voltage output as a function of time in Volts, μ_0 is the vacuum permeability in Vs/Am, I is the current amplitude in Ampère and finally t is the time after transmitter power-off.

Early and late times may be differentiated through the time dependent parameter τ. It is given by Zhdanov (2009) as

$$\tau = \frac{t}{\mu_0 \sigma R^2} \tag{10}$$

where σ represents the conductivity in S/m as the inverse of resistivity. Early times are considered for $0 < \tau < 1$ and late times for $\tau \to \infty$. Model calculations are based on the late time approach only, as data for early times smaller than approximately 10^{-2} ms – with a corresponding $\tau < 1$ for $\mu_0 = 4\pi \cdot 10^{-7}$ Vs/Am, $\sigma = 0.01$ S/m assuming semi-conductive sediments and $R = 50$ m for the employed geometric layout of the TEM installation – show significant scattering and are therefore discarded. It has to be kept in mind that the visualization of response curves might not appear as intuitive as MT curves and be misleading.

3.2. Data collection

In total 29 MT and 23 TEM stations were placed along a major profile running from SW to NE and two smaller profiles, one parallel, one perpendicular, within the Profeta basin (see Fig. 1). Two Metronix ADU-07 measurement units, MFS-07 coils and $PbCl_2$ electrodes were used for the MT data and the ABEM WalkTEM was employed as the according equipment for TEM data acquisition. Each MT station recorded 5 channels (three magnetic and two electric field components) with sampling frequencies of 128 Hz for 12 h and 40 min at 4096 Hz. Stations MT22 to MT29, however, had to be reduced to 4 h and 20 min as one measurement unit failed during the survey. TEM measurements were conducted with a central loop installation using a square transmitter of 100 m × 100 m, enclosing two receivers of 1 m × 1 m and 10 m × 10 m, respectively. Impulse currents of 1 A and 10 A were chosen to achieve different penetration depths. Usually 35 stacks were used to generate a data set ('sweep'), but it turned out that only the larger current was of sufficient quality for a successful modeling. Data from the small and the large receiver coils are termed sweep 3 and sweep 4 in the following.

4. 1-D TEM inversion

The TEM data were inverted by employing the commercial IX1Dv3 software (Interpex Ltd). Produced TEM 1-D models all yield reasonable model responses with adequate fits and RMS values smaller than 5%. Exemplary sites TEM01 and TEM05 shall be discussed in detail. As seen in Fig. 2, response curves fit the data quite well and the equivalence of the models (indicated by dotted green lines) keeps within adequate limits. TEM model visualizations will only account for the late time apparent resistivity curves as they generate a more easily interpreted graphic image of the data. As employed so far, warm colors represent higher conductivities and colder colors higher resistivities in the context of MT models. Hydrogeological approaches, however, commonly make use of levels of gray, which is why the 1-D TEM models within the following chapter will use light gray colors for conductors and the associated aquifer structures and darker shades for dry sediments and basement.

Almost all models yield a top layer with intermediate resistivities of approximately 100 Ωm associated with a sedimentary topset bed. In depths of 30 m highly conductive features of 10 Ωm can be found at almost every site (compare Figs. 2 and 3). Only at sites TEM16 (Fig. 4), TEM22 and TEM23, at the very ends of the profile and quite far away from the basin center, highly resistive features over 200 Ωm, associated with the basement, can be confidently recognized.

So in conclusion, the TEM results quite confidently map the top of the aquifer system under investigation. The lower boundary of the aquifer or the top of the basement could not be resolved, however. Combining all models from the 1-D inversions a simplified image of the subsurface can be visualized by bar graphs, as visualized in Fig. 5.

As the given apparent resistivities merely represent an averaged value of the whole formation under investigation, it is of interest to give an estimate for the resistivity of the contained fluids. This can be achieved by making use of *Archie*'s law (Archie, 1942):

$$\rho_0 = F\,\rho_f = a\,\Phi^{-m}\,S^{-n}\,\rho_f \tag{11}$$

with the formation factor F and where ρ_0 and ρ_f represent formation and fluid resistivity, respectively, Φ is porosity and S saturation, a is an empirical factor around 1 and the cementation exponent m

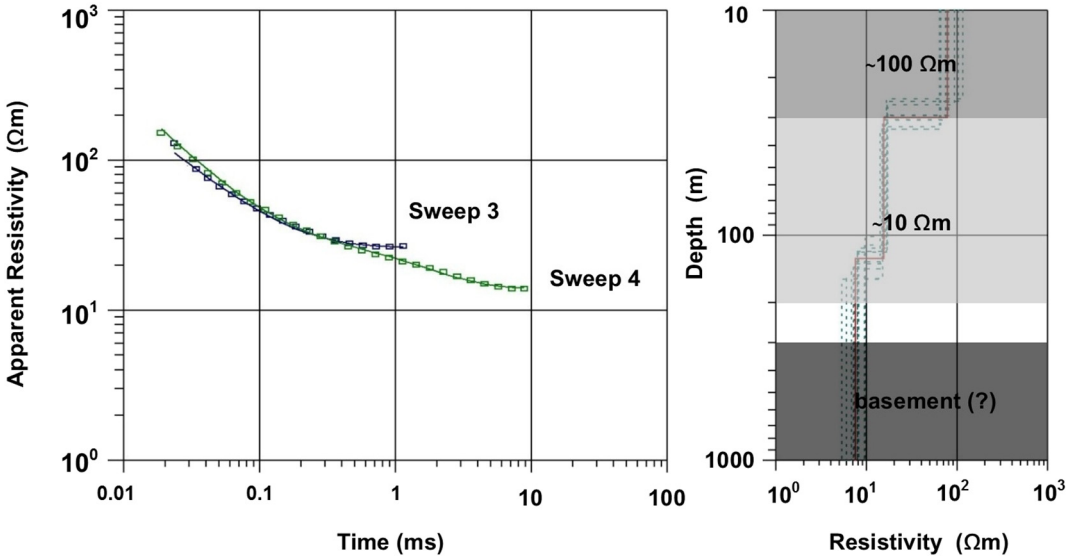

Fig. 2. Late time apparent resistivity curves at site TEM01 for sweeps 3 and 4 with an impulse current of 10 A. Transmitter loop was a square with 100 m side length, receiver coil sizes were 10 m × 10 m and 1 m × 1 m in an in-loop configuration. Fit of model response achieved an RMS of 4.82%. The depth of the resistive basement was only included from geological reasoning, but note that this is not seen in the TEM data.

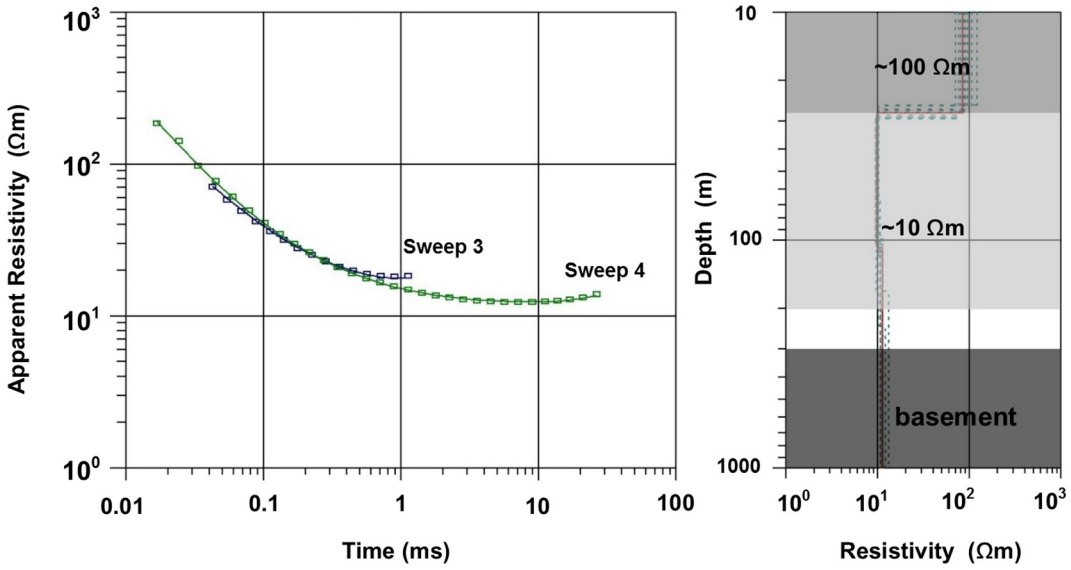

Fig. 3. Late time apparent resistivity curves at site TEM05 for sweeps 3 and 4 with an impulse current of 10 A for receiver coil sizes of 10 m × 10 m and 1 m × 1 m. RMS = 2.57%. Basement depth is set as for the data in Fig. 2.

is usually assumed to lie within the range of $m = 1.3–2.5$ (Mavko et al., 2009). The saturation exponent n (often set to 2) is unimportant for full saturation with S = 1, as assumed in the following. Presupposing a formation resistivity of 10 Ωm as indicated by the TEM data, assuming porosities between 5% and a maximum of 20%, and varying the range of the empirical factors a and m, a fluid resistivity within the range of 0.15 and 2.31 Ωm can be hypothesized, suggesting fluids of highly saline character in the subsurface. There is no indication of significant clay layers from geological maps and lithology which would alter these values.

5. Joint 1-D TEM and MT response examination

Multiple stations with overlapping coordinates were chosen from the profile to directly compare 1-D TEM and MT inversion results. The TEM data were again inverted with IX1Dv3, while the MT data were analyzed with the WinGLink software package (Schlumberger Ltd.). For the 1-D approximation we chose the Berdichevsky invariant, involving the geometrical average of the minor impedance diagonal (see a recent discussion on invariants by Rung-Arunwan et al., 2016).

Assuming a three-layer case (with a top layer of intermediate resistivity, a highly conductive aquifer and the underlying highly resistive basement), 1-D TEM model parameters were used to calculate the forward MT response, and vice versa. First attempts used TEM data responses and incorporated the MT results, shown in Fig. 6. The invariants of the impedance were used to create the 1-D MT models and in order to keep TEM and MT comparable, a three-layer case was assumed, incorporating again a top layer of intermediate resistivity, a conductive aquifer and the underlying resistive

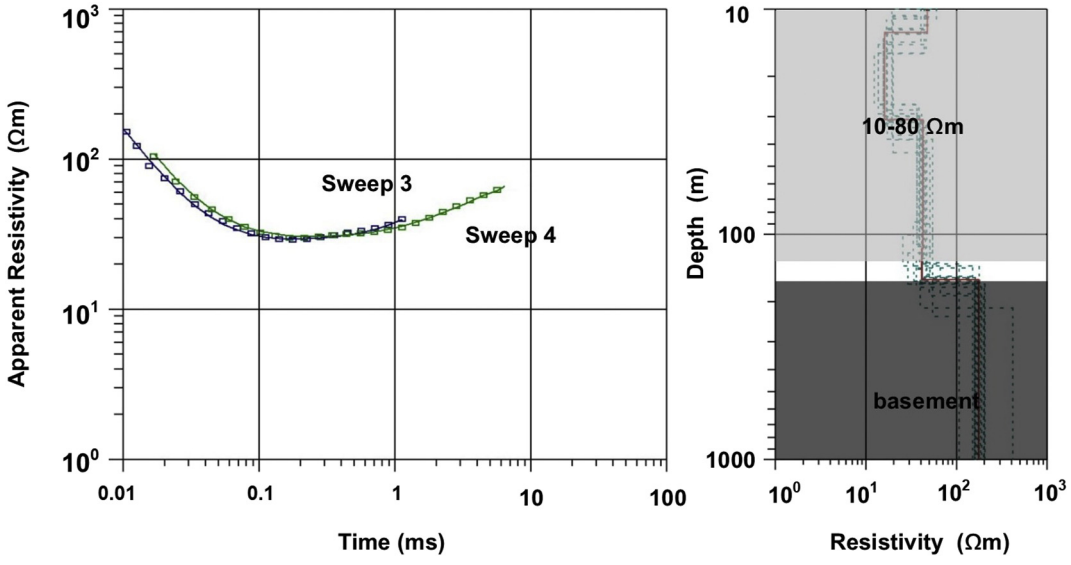

Fig. 4. Data for site TEM16 at the margin of the basin, where the basement depth is better resolved than in the examples before. RMS = 4.37%.

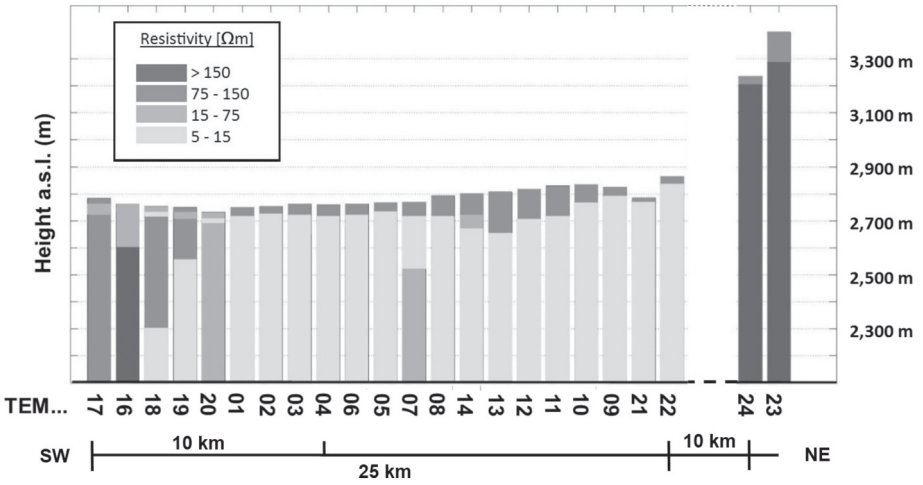

Fig. 5. A simplified image of the resistivity distribution, generated from the 1-D TEM model parameters. Light gray colors represent conductive, dark colors resistive structures. Basement can only be identified at the edges of the basin at TEM sites 16, 23 and 24. The quite peculiar higher resistive feature at site TEM07, apparently somehow separating the saturated layers, actually can be found in MT inversion results as well and might be related to outcrops from S-N striking Cenozoic basement as visible in the geological overview (Fig. 1).

basement. Adequate responses, however, cannot be achieved in this manner for all sites. Model responses agree tolerably well, although MT 1-D results are mapping higher conductivities and therefore response curves are shifted.

Reconciliation of the particular results somewhat improves when considering the influence of galvanic distortion on the MT data. Small and shallow conductivity anomalies cause static effects at boundary surfaces and result in a down- or upscaling of the electric field and therefore the apparent resistivity (e.g., Jones, 2012). This very shift can be observed preeminently in the data from MT05 compared to TEM08 and is visualized in more detail in Fig. 7.

TEM is sometimes seen as a measure to overcome static shift in magnetotellurics (see, e.g., Pellerin and Hohmann, 1990). However, this works only under otherwise 1-D conditions, and/or if the TEM soundings allow a spatial resolution of the surroundings of the measuring site. An impedance invariant may be used, but this only averages the data and may lead to wrong models. We thus skip this point here and come back to the static shift problem when dealing with 2-D and 3-D inversion.

6. 3-D MT inversion

The common procedure in analysis of MT data is to check for dimensionality and electrical strike angle with the implicit hope that impedances are sufficiently two-dimensional so that a 2-D inversion is adequate, which will save time and computing resources when compared with a full 3-D approach. But a brief look at phase tensors and their skew angle β (Caldwell et al., 2004) makes a 2-D analysis obsolete for our data (not shown here). Furthermore, induction arrows at several sites (where available) clearly indicate the three-dimensionality of the subsurface: Arrows point perpendicularly away from the main profile (Fig. 8) and are not consistent with the geological strike visible in the map (Fig. 1).

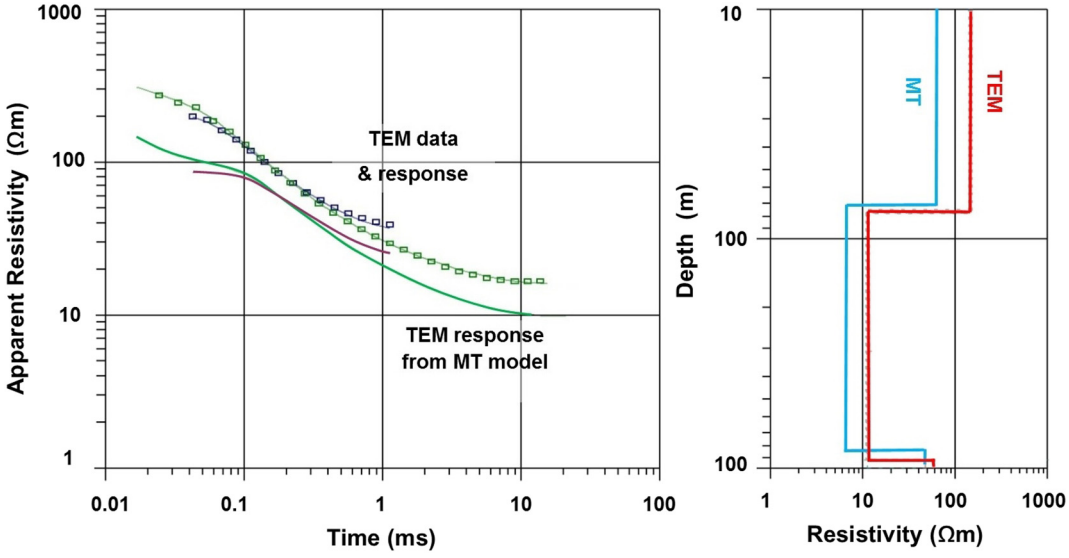

Fig. 6. Comparison of TEM and MT 1-D inversions for the common sites TEM08 and MT05. Right: Best fitting independent 1-D models for a three-layer case, displayed by red and blue curves for TEM and MT, respectively. Left: TEM data and responses (rectangles and pale curves) and TEM response resulting from forward modeling of the MT model (thick curves).

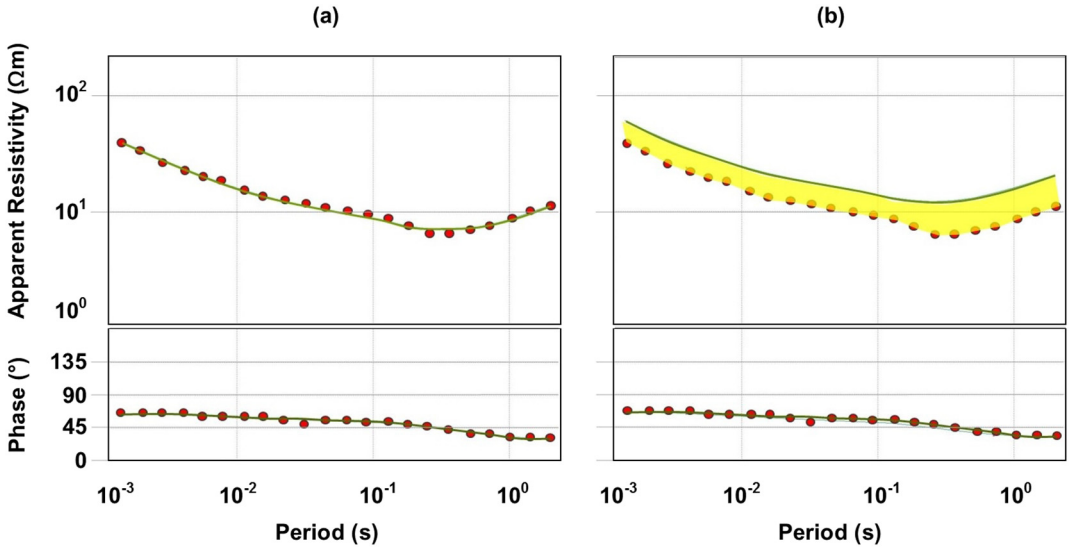

Fig. 7. MT05 data and response curve from 1-D inversion and forward response for 1-D TEM model parameters. (a): MT05 data (invariant, red dots) and response (green line). (b): MT05 data and TEM response. As already shown in Fig. 5, model responses or apparent resistivity curves respectively feature similar trends, are shifted though where phases stay identical. This effect is known as static shift. Magnitude of shift indicated by yellow zone. As a result MT images higher conductivities.

As most data display 3-D characteristics, several modeling runs were performed with different combinations of transfer functions, employing the ModEM 3-D inversion code of Egbert and Kelbert (2012). The data from the vertical magnetic component were missing for several sites and of insufficient quality for many of the remaining stations. Ultimately, they were excluded from the inversion as no sufficient fit could be achieved. Disregarding of main diagonal and vertical magnetic components and gradual adjustment of crucial inversion parameters such as cell dimension, grid size and spacing, finally led to satisfactory results and a decent fit could be achieved. The final model comprises nx=67, ny=98 and nz=40 cells; model dimension is 1400 km in horizontal and 600 km in vertical directions and model covariance was 0.3 throughout the model domain. Selected slices in plan view are illustrated in Fig. 9. Fig. 10 shows selected responses for the major profile A as well as the corresponding model as cross-section.

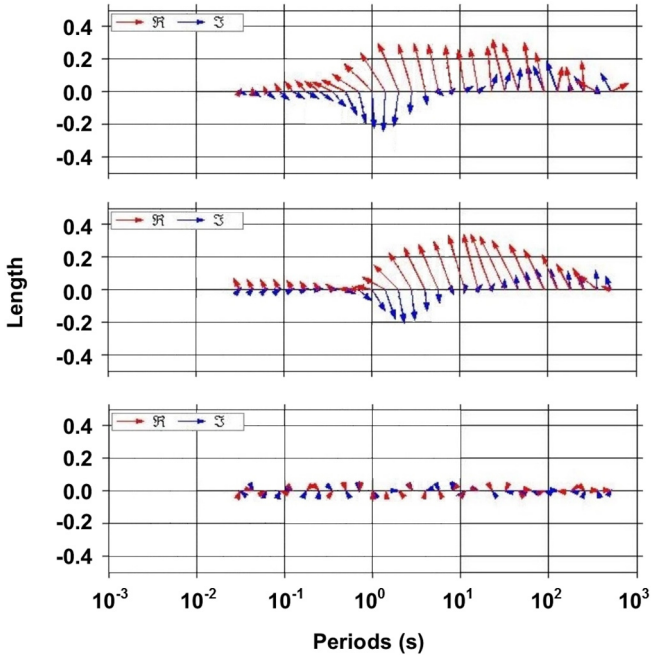

Fig. 8. From top to bottom: induction arrows of sites MT03, MT18 and MT19 in the 128 Hz sampling frequency domain. Red arrows represent the real, blue arrows the imaginary part of the tipper. Data quality at MT03 and MT18 is overall satisfying, with the exception of the longest periods. Note that arrows point away from the profile which was laid out in SW-NE direction. At MT19 vectors are very small, indicating an 1-D subsoil. Overall quality of induction arrows, however, denote most of the tipper data useless.

Model responses fit the data reasonably well, yielding an RMS for the residual of 1.497 on the basis of an error floor of 5% for the impedance elements. Data of some stations indicate three-layer cases, showing corresponding curves with high resistivities of 100 Ωm for short periods, proceeding to much smaller resistivities of 10 Ωm and again ending in higher resistivities for long periods. Most sites, however, only map a highly resistive top layer and a highly conductive bottom layer.

Several sensitivity tests (by setting certain conductive structures to the value of the environment and starting inversion over) support the imaged conductivity distribution, as all major features appear necessary to explain the data. Other attempts included variations of the starting model, e.g., an a-priori built-in basement of 1000 Ωm, beginning at 600 m. The inversion result again produces most of the structures as shown in the models with a RMS of 1.665, but with a poor fit at long periods. Further tests comprised variation of the model covariance; in terms of a trade-off, the chosen value of 0.3 as in the plotted model of Figs. 9 and 10 can be seen as a compromise between “too rough and too smooth”.

Highly conductive features associated with saturated layers can be identified at least until depths of 1.5 km, showing strongest occurrences from 120 to 600 m especially in the north-eastern part within profile A, which is supposed to somewhat represent the center of the basin (compare Fig. 9). The top of the aquifer seems to be imaged already within the first 20 m of depth, which actually agrees with the results from the TEM data. The majority of the sites however, suggest a top at approximately 200 m depth, better perceptible when incorporating the cross-section, Fig. 10. The resistivities may be biased as a result of static shift as already discussed earlier. MT results therefore might image higher conductivities than expected. More details

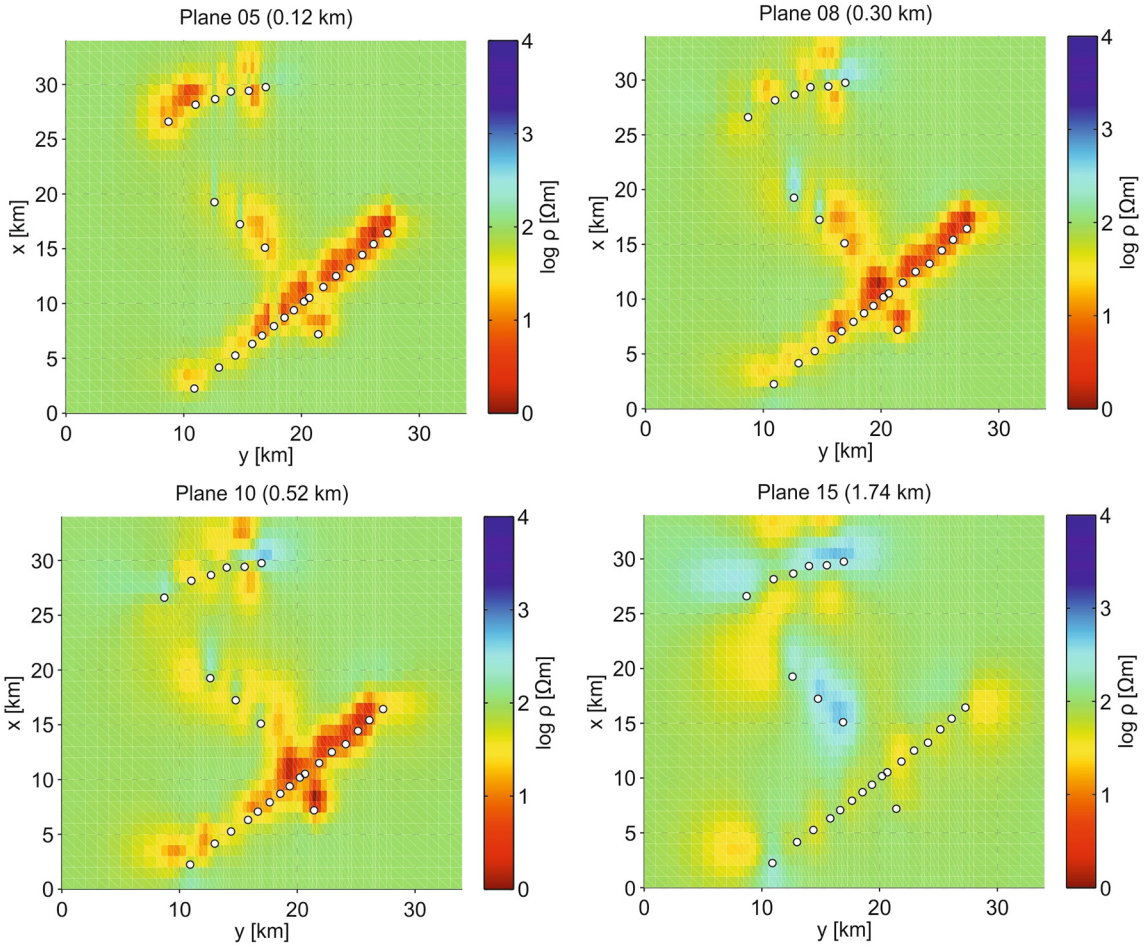

Fig. 9. Plan view slices for significant depths from the 3-D model. Good conductors, indicated by red to orange colors, are present especially in the north-eastern part along profile A, as well as at shallow depths along profile C, at lower altitudes. Conductive features are visible until depths of more than 1.5 km within the assumed area of the center of the basin. The higher resistive features of blue and turquoise colors, appearing in depths of 1.74 km are presumed to be artifacts from the inversion and are not considered as significant. Inversion parameters: smoothness factor (model covariance) of 0.3, 5% error floor, RMS = 1.493. Sensitivity tests support the imaged conductivity distribution, as all major features appear necessary to explain the data.

concerning inversion experiments with TEM and MT data may be found in Ruthsatz (2017).

3-D inversions of data sets with insufficient spacial coverage sometimes display artifacts in areas (model domains) where no sites are present. As is visible from Fig. 9, this is not the case here for the relevant, relatively short periods: major off-profile features do not exist in the model sections; large areas remain at the value of the starting model (100 Ωm, green color).

Distinct, sharp boundaries between topset bed, aquifer and basement can actually not be identified, they ought not to be precisely defined though. As suggested by the geological setting, the basement is supposed to consist of sediments which most likely possess a weathered top layer and are characterized by numerous faults and sediment filled fractures. An unambiguous boundary therefore cannot be expected as the transition from aquifer to surrounding rock is elusive and rather indistinct. To the same degree, a confident top of the aquifer cannot be inferred as evidently compared to the TEM data. Furthermore, the heavy rain during the beginning of the year (Jordan et al., 2015) in particular might bias the results as uncertain quantities might have been trapped within shallow layers. Actually, no reliable data regarding basement depths, from inter alia drilling, are available at this point. Therefore no confident top and bottom depths for saturated layers can support or oppose the results.

7. Conclusions

Overall, MT and TEM results agree reasonably well when considering the observed static shift effects in the MT data. TEM data obviously seem to better identify the top of the aquifer under investigation, where especially 3-D MT models yield a more complex solution. Generally the top of fluid-saturated layers can be assumed to lie within the first 20 to 100 m of depth. Both methods suggest a mean apparent resistivity of the aquifer around 10 Ωm, which translates to 0.3–2.3 Ωm of fluid resistivity when applying Archie's law. These values indicate fluids of very saline character, what might be explained by high evaporation under the arid conditions in the region of the Andean mountains. Note that the source region of the high Andes are characterized by numerous salars (salt pans). Especially after the strong rains in early 2015 exceeding 40 mm during one day, as reported in Bozkurt et al. (2016), one might want to consider their effect with caution. Remaining humidity may reduce resistivity of the uppermost layers, but this remains uncertain.

The basin itself appears much deeper in the North-East, and much shallower in the South-West and North, suggesting an asymmetric structure. A distinct, sharp top of the basement can actually not be identified. As suggested by the geological setting, the basement itself consists of probably eroded and fractured volcanic-pyroclastic sediments, allowing for the intrusion of fluids into the top layers. An

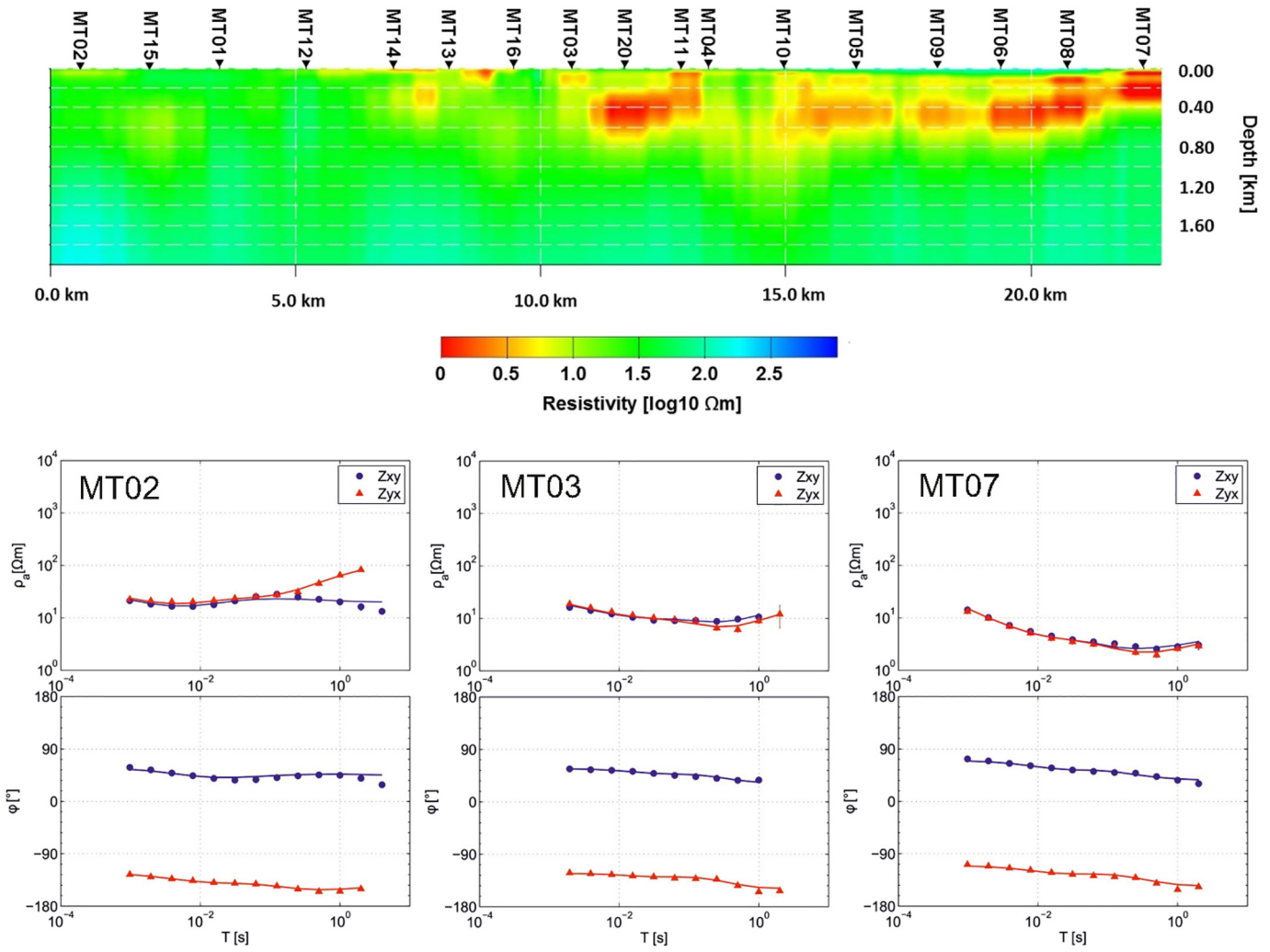

Fig. 10. 3-D model (vertically exaggerated by a factor of 2) and selected responses from the major SW-NE-profile after 50 iterations. Inversion parameters: smoothness factor of 0.3, 5% error floor, RMS = 1.497. Data and estimate almost depict a "rope of beads", as is desired as it represents small deviations between the original data and the hypothetical data calculated for the model estimates. Error bars are not visible as they lie within the dimensions of the symbol size.

unambiguous boundary therefore cannot be expected as the transition from aquifer to surrounding rock is elusive and rather indistinct. Generally, it would be hard to distinguish a somehow weathered layer of intermediate resistivity on top of the resistive basement, as we also proved with several forward calculations, e.g., at site TEM16. This is an expression of the well-known principle of layer suppression, evident not only in TEM, but also in MT and geoelectrics.

Furthermore, both in the TEM and MT data, a separation of the aquiferous layers can be observed between MT04 and MT10 as well as in TEM07. Allowing for the geomorphological aspects of the area as visualized in Fig. 1, this might be explained by the northern outcrop of the Pre-Cenozoic basement. This dominant feature might actually continue from North to South, dividing the saturated layers within the center of the basin as a structural boundary.

Acknowledgments

This research was funded by the National Commission for Scientific and Technological Research of Chile (CONICYT), through Project ACT 1203: Exploration and Assessment of New Groundwater Resources in the Central Depression of Antofagasta Region.

We thank Gary Egbert, Anna Kelbert and Naser Meqbel for providing the 3-D inversion code, Barbara Blanco for her support in the field and her part in the TEM data processing, Gerhard Kapinos for discussions on TEM model appraisal and the Andean Geothermal Center of Excellence (CEGA, FONDAP-CONICYT 15090013) for supporting us with the MT equipment. Michael Becken supplied his processing code for the MT data and Naser Meqbel his graphic 3-D model and data editing tool. We thank two reviewers for their comments which helped to improve the manuscript.

References

Archie, G.E., 1942. The electrical resistivity log as an aid in determining some reservoir characteristics. Trans. AIME 146. https://doi.org/10.2118/942054-G.

Bozkurt, D., Rondanelli, R., Garreaud, R., Arriagada, A., 2016. Impact of warmer eastern tropical Pacific SST on the March 2015 Atacama Flood, Monthly Weather Report. Am. Meteorol. Soc. https://doi.org/10.1175/MWR-D-16-0041.1.

Caldwell, T.G., Bibby, H.M., Brown, C., 2004. The magnetotelluric phase tensor. Geophys. J. Int. 158, 457–469.

Charrier, R., Pinto, L., Rodríguez, M., 2007. Tectono-Stratigraphic Evolution of the Andean Orogen in Chile, Geology of Chile. The Geological Society, London. Chapter 3.

Chong, G., 1977. Contribution to the knowledge of the Domeyko Range in the Andes of northern Chile. Geol. Rundsch. 66, 374–404.

Chong, G., von Hillebrandt, A., 1985. El Triásico preandino de Chile entre los 23°30 y 26°00 de lat. Sur. Actas 4° Congreso Geológico Chileno, Antofagasta. 1, 138–154.

DGA, 2012. Dirección General De Aguas. Diagnóstico Plan Estratégico para la gestión de los recursos hídricos, Región de Antofagasta,

Egbert, G.D., Kelbert, A., 2012. Computational recipes for electromagnetic inverse problems. Geophys. J. Int. 189, 251–267.
Espinoza, F., Matthews, S., Cornejo, P., 2012. Carta Los Vientos, Región de Antofagasta, Servicio Nacional de Geología y Minería, Carta Geológica de Chile. Serie Geología Básica No. 138: 72 p., scale of 1:100.000.
Espinoza, F., Matthews, S., Cornejo, P., Venegas, C., 2011. Carta Catalina, Región de Antofagasta, Servicio de Geología y Minería, Carta Geológica de Chile. Serie Geología Básica No.129: 63p., scale of 1:100.000.
Fernández-Mort, A., Riquelme, R., Muñoz, S., Centellas, K., 2015. Cenozoic sedimentary and palaeogeographic evolution of the Quebrada Del Profeta Basin, northern Chile, IX Congreso Geológico de España. Geo-Temas 16 (2). ISSN 1576-5172.
Gamboa, C., 2014. Evaluación del flujo de aguas subterráneas en el flanco occidental de la Cordillera de Domeyko en el área comprendida entre las coordenadas UTM 7.214.000-7.228.000 N y 435.000-466.000 E. Región de Antofagasta, memoria para optar al título de Geólogo. Universidad Católica del Norte.
González, R., Wilke, G.-H., Menzies, A.H., Riquelme, R., Herrera, C., Matthews, S., Espinoza, F., Cornejo, P., 2015. Carta Sierra de Varas, Región de Antofagasta, Servicio Nacional de Geología y Minería, Carta Geológica de Chile. Serie Geología Básica, scale of 1:100.000.
Herrera, C., Custodio, E., 2014. Origin of waters from small springs located at the northern coast of Chile, in the vicinity of Antofagasta. Andean Geol. 41 (2), 314–341.
Herrera, C., Porrout, P., Chong, G., 1997. Caracterización hidrogeológica de la Cordillera de Domeyko. VIII Congreso Geológico Chileno, Antofagasta.
Jones, A.G., 2012. Distortion of magnetotelluric data: its identification and removal. In: Chave, A.D., Jones, A.G. (Eds.), The Magnetotelluric Method, Theory and Practice. Cambridge Univ. Press., pp. 219–302.
Jordan, T., Riquelme, R., González, G., Herrera, C., Godfrey, L., Colucci, S., Gironáas León, J., Gamboa, C., Urrutia, J., Tapia, L., Centella, K., Ramos, H., 2015. Hydrological and geomorphological consequences of the extreme precipitation event of 24–26 March 2015, Chile, ext. abstract. XIV Congreso Geológico Chileno, La Serena.
Mavko, G., Mukerji, T., Dvorkin, J., 2009. The Rock Physics Handbook: Tools for Seismic Analysis in Porous Media. 2nd ed., Cambridge Univ. Press, Cambridge.
Pellerin, L., Hohmann, G., 1990. Transient electromagnetic inversion: a remedy for magnetotelluric static shifts. Geophysics 55 (9), 1242–1250.
Reutter, K., Scheuber, E., Helmcke, D., 1991. Structural evidence of orogen parallel strike-slip displacements in the North Chilean Precordillera. Geol. Rundsch. 80, 135–153.
Rung-Arunwan, T., Siripunvaraporn, W., Utada, H., 2016. On the Berdichevsky average. Phys. Earth Planet. Inter. 253, 1–4.
Ruthsatz, A.D., 2017. Joint Conductivity Imaging of TEM and MT Data, Profeta Basin, North Chile.Master Thesis. Freie Universität, Berlin, Fachrichtung Geophysik.
UN-Water Country Brief Chile, 2013. Food and Agriculture Organization (FAO). AQUASTAT Programme, United Nations.
Venegas, C., Cervetto, M., Astudillo, N., Espinoza, F., Cornejo, P., Mpodozis, C., Rivera, O., 2013. Carta Sierra Vaquillas Altas, Regiones de Antofagasta y Atacama, Servicio Nacional de Geología y Minería, Carta Geológica de Chile. Serie Geología Básica 159., scale of 1:100.000.
Zhdanov, M.S., 2009. Geophysical Electromagnetic Theory and Methods. Methods in Geochemistry and Geophysics, 43. Elsevier B.V., Amsterdam.